ELSEVIER

International Journal of Fatigue 23 (2001) S413–S421

International Journal of Fatigue

www.elsevier.com/locate/ijfatigue

Foreign-object damage and high-cycle fatigue: role of microstructure in Ti–6Al–4V

J.O. Peters, R.O. Ritchie *

Department of Materials Science and Engineering, University of California, Berkeley, CA 94720-1760, USA

Abstract

The objective of this study was to evaluate the influence of microstructure on the susceptibility to high-cycle fatigue (HCF) failure in Ti–6Al–4V following foreign-object damage (FOD), specifically by comparing a fine-grained bi-modal microstructure with a coarse grained lamellar microstructure. FOD was simulated by high-velocity impacts of steel spheres on a flat surface. This caused a marked reduction in the smooth-bar fatigue strength in both microstructures, primarily because of the premature initiation of fatigue cracking resulting from the stress concentration associated with damage site and FOD-induced microcracking. The FOD-initiated microcracks were found to be of a size comparable with microstructural dimensions, and on subsequent fatigue loading were seen to propagate at applied stress-intensity levels below $\Delta K \sim 1$ MPa $m^{1/2}$, i.e. a factor of roughly two less than the 'worst-case' threshold stress-intensity range in Ti–6Al–4V for a crack of large size compared to microstructural dimensions (a 'continuum-sized' crack). A rational approach against HCF failures from such microcracks is proposed for the fine-grained bi-modal microstructure based on the Kitagawa–Takahashi diagram. For the bi-modal microstructure, the Kitagawa–Takahashi diagram provides a basis for describing the threshold conditions for FOD-induced HCF failures, in terms of the *stress concentration corrected* smooth-bar fatigue limit for small crack sizes and the worst-case threshold for larger continuum-sized cracks. However, this approach was found to be less applicable to the coarse grained lamellar microstructure, primarily because of low small-crack growth resistance relative to its higher smooth-bar fatigue limit.

Keywords: Foreign-object damage; High-cycle fatigue; Fatigue-crack growth threshold; Small cracks; Ti–6Al–4V

1. Introduction

Because of an increasing number of incidents of high-cycle fatigue (HCF) related jet engine failures of military aircraft, currently used HCF design methodologies, based on stress-life (S–N) curves and the Goodman diagram, are being re-evaluated [1–3]. Both foreign-object damage (FOD) from hard body impacts (e.g. debris ingested from the runway into the inlet of a jet engine, which can primarily damage the leading edge of fan blades) and fretting (e.g. particularly in the blade dovetail/disk sections) are identified as critical problems [1–3], which can lead to premature fatigue crack initiation and subsequent crack growth. This in turn can result in seemingly unpredictable *in service* failures, due to the high-frequency vibratory loading (>1 kHz) involved [3]. Even cracks growing at slow per-cycle velocities of $\sim 10^{-10}$ m/cycle can propagate to failure in a short time period. In light of this, design against HCF based on the damage-tolerant concept of a fatigue-crack growth threshold (ΔK_{TH}) for no crack growth would appear to offer a preferred approach; however, such thresholds must reflect representative HCF conditions of small crack sizes, high frequencies and high mean stress levels (depending on the blade span location) [1–5].

As a basis for such an approach, past studies have been focused on the role of FOD in affecting the initiation and early growth of small surface fatigue cracks under HCF conditions in fan blade processed Ti–6Al–4V alloy with fine-grained bi-modal microstructure[1] [6–10]. The prime effect of FOD in markedly lowering resistance to HCF was found to be due to earlier crack initiation. Specifically, premature crack initiation and

* Corresponding author. Tel.: +1-510-486-5798; fax: +1-510-486-4881.

E-mail address: roritchie@lbl.gov (R.O. Ritchie).

[1] This microstructural condition has also been termed solution treated and overaged (STOA).

0142-1123/01/$ - see front matter
PII: S0142-1123(01)00168-2

subsequent near-threshold crack growth were promoted by the stress concentration associated with the FOD indentation [6–9] and the presence of ('microstructurally') small cracks [7,10] in the damaged zone; in addition, residual stress gradients [6,7,9] and microstructural changes [6,7] due to FOD-induced plastic deformation play an important role. Limiting conditions for potential HCF-related turbine failures were proposed based on the concept of a 'worst-case' threshold for no fatigue crack growth, an approach that strictly applies for 'continuum-sized' cracks, i.e. large or physically small cracks with dimensions larger than the characteristic microstructural size-scales. However, in the presence of *microstructurally* small cracks at FOD indentation site, limiting threshold conditions for crack growth were alternatively defined in terms of *stress concentration corrected* stress ranges in the context of the Kitagawa–Takahashi diagram [11]. To provide limiting criteria for HCF failures using this approach, the threshold conditions were described in terms of the smooth-bar fatigue limit (at microstructurally small crack sizes) and worst-case large-crack fatigue threshold (at larger, continuum-sized, crack sizes) [7].

The purpose of the present study is to examine the influence of microstructural dimensions on the fatigue crack initiation and early fatigue crack growth from FOD-induced microcracks by comparing fine-grained bi-modal microstructure with coarser grained β annealed lamellar microstructure. In contrast to the bi-modal microstructure where FOD-induced microcracks ($2c$~2–50 μm) are of comparable dimensions to the fine-grained bi-modal microstructure, in the lamellar microstructure such microcracks are far smaller than the average lamellar colony size (~500 μm).

2. Experimental procedures

The Ti–6Al–4V alloy (Ti–6.3Al–4.2V–0.2Fe–0.2O, wt.%) in the bi-modal microstructural condition was part of a set of forgings produced specifically for the U.S. Air Force sponsored programs on HCF. Mill annealed 63.5 mm diameter bar stock material was α+β forged to a plate size of 400×150×20 mm^3. Subsequently, the forging plates were solution treated (below the β-transus of ~996°C) at 927°C for 1 h followed by fan air cooling. Finally, the plates were stress relieved for 2 h at 705°C. Additional material and processing details are given in Ref. [12]. The resulting bi-modal microstructure of the plate material, consisting of a volume fraction of ~60% primary α (diameter ~20 μm) within a lamellar α+β matrix, is shown in Fig. 1(a). To obtain a fully lamellar microstructure for comparison, specimen blanks (20×20×90 mm^3) of bi-modal plate material were β annealed at 1050°C for 30 min and subsequently cooled by a He-quench (cooling rate of ~100°C/min). Finally,

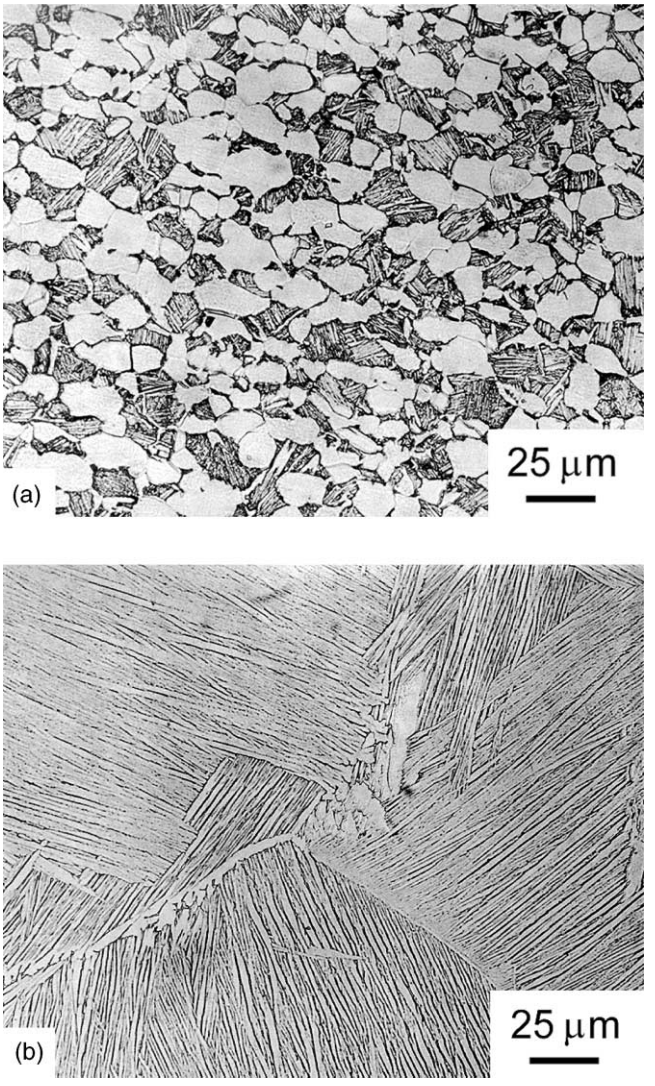

Fig. 1. Microstructures of Ti–6Al–4V: (a) bi-modal (solution treated and overaged, STOA) and lamellar (β annealed).

the blanks received the same stress relief treatment as bi-modal plate material (2 h at 705°C). The lamellar microstructure shown in Fig. 1(b) exhibited a β grain size of ~1000 μm, a colony size (parallel oriented α phase plates) of ~500 μm and lamellae thickness of ~1 μm, corresponding to the lamellae thickness of the bi-modal microstructure. Uniaxial tensile properties (based on testing performed parallel to the length of the plate at an initial strain rate of 8×10^{-4} s^{-1}) are listed in Table 1. The slightly higher yield stress of 975 MPa of

Table 1
Uniaxial tensile properties of Ti–6Al–4V. $\sigma_{0.2}$: yield stress, UTS: ultimate tensile strength, TE: tensile elongation, RA: reduction of area at fracture; strain rate 8×10^{-4} s^{-1}

Microstructure	$\sigma_{0.2}$ (MPa)	UTS (MPa)	TE (%)	RA (%)
Bi-modal	915	965	19	45
Lamellar	975	1055	12	10

the lamellar microstructure, as compared to 915 MPa of the bi-modal microstructure, is presumably due to higher cooling rate from solution treatment temperature. The markedly higher ductility of the bi-modal condition (reduction in area, RA=45%), compared to the lamellar condition (RA=10%), can be attributed to the much smaller grain size limiting the effective slip length.

In addition to the stress-life (S–N) data taken for bi-modal Ti–6Al–4V from Ref. [13] (for $N_f<2\times10^7$ cycles), S–N tests were performed on hourglass specimens (diameter: 5.4 mm) at 1000 Hz to provide an evaluation of the smooth-bar HCF limit of the Ti–6Al–4V alloy with bi-modal and lamellar structures. To minimize surface residual stresses and the high-dislocation density from specimen processing, specimen surfaces were chemically milled after machining. The specimen axis was oriented parallel to the length of the plate (*L*-direction).

The effect of FOD on the fatigue behavior of Ti–6Al–4V was examined using modified K_B specimens. This sample has a rectangular cross-section of 3.2 mm by 7.2 mm, a gauge length of 20 mm and cylindrical buttonhead grips. A nominally stress-free surface in the gauge section was prepared using standard stress relief and chemical-milling procedures. FOD was simulated by firing 3.2 mm diameter chrome-hardened steel spheres onto a flat specimen surface of tensile fatigue (modified K_B) specimens at an angle of 90° at velocities of 200–300 m/s using a compressed-gas gun facility. Further details of the FOD simulation are given in Ref. [6]. After impact, specimens were cycled (sinusoidal waveform) at load ratios of R=0.1 and 0.5. Throughout fatigue testing, specimens were periodically removed from the test frame and the progress of crack initiation and growth examined in a high-resolution LEO 1550 field-emission scanning electron microscope (SEM).

Approximate local stress intensities for small cracks at base and crater rim of the indentation were calculated from the relationship of Lukáš [14] for small cracks at notches, in terms of elastic stress-concentration factor (k_t) surrounding the indentation site [15], stress range ($\Delta\sigma$), crack depth (a), and indentation radius (ρ). The factor of 0.7 is based on the stress-intensity boundary correction and the crack-shape correction factors [16]

$$\Delta K=\frac{0.7\,k_t}{\sqrt{1+4.5(a/\rho)}}\Delta\sigma\sqrt{\pi a} \quad (1)$$

It should be noted here that there are some uncertainties in the calculation of the driving forces for the propagation of FOD-initiated microcracks ($2c$~2–50 μm), specifically because of their size in relation to the scale of local plasticity (although maximum plastic zone sizes are only roughly 1/5–1/10 of the crack length, i.e. in the order of ~0.2–1 μm for 1–10 μm sized cracks at ΔK~1–2 MPa $m^{1/2}$), and because of the presence of both tensile and compressive residual stresses in the vicinity of the indents. Eq. (1) does not take into account the presence of residual stresses, as to the first approximation such stresses will not change the value of the stress-intensity range (ΔK); they do, however, affect the mean stress and hence alter the local load ratio. The magnitudes of these stresses in the vicinity of the damage site are currently being computed and experimentally measured [17,18], as briefly discussed below. Indeed, the local residual stresses at the base and rim of the FOD indents have been shown in many cases to relax, or redistribute under cyclic loading, specifically at applied stresses comparable with the 10^7-cycle smooth-bar fatigue limit, i.e. ~500 MPa, which was used in the present work.

3. Results and discussion

3.1. Simulation of FOD

Impact damage sites caused by 300 m/s normal impacts on flat surfaces are shown in Fig. 2(a) and (b) for the bi-modal and lamellar microstructure, respectively. Increasing states of damage have been reported with increasing impact velocity for the bi-modal microstructure [6,7]. In particular, above a 250 m/s impact velocity, pile-up of material occurred at the crater rim with an associated presence of micronotches and microcracks; moreover, circumferentially oriented intense shear bands were formed, emanating from the surface of the impact crater. Such effects were not apparent for 200 m/s impacts. A comparable increase in damage with increasing impact velocity was seen in the lamellar microstructure, although the occurrence of the crater rim pile-up and associated micronotch and microcrack formation were more severe (compare Fig. 2(a) and (b)). However, for the impact velocities of 300 m/s, the sizes of the FOD-induced microcracks were comparable, i.e. ~2–50 μm in surface length, for both bi-modal and lamellar microstructures. When favorably oriented to the subsequently applied fatigue stress axis, such microcracks provided the preferred nucleation sites for fatigue-crack growth, as shown in Fig. 3(a) and (b) for the bi-modal and lamellar microstructures, respectively. However, as such microcracking was absent for impact velocities below 250 m/s, it is clear that low velocity or quasi-static indentations do not provide a realistic simulation of FOD.

Additionally of importance for crack initiation was the observation of tensile residual stresses (~300 MPa in longitudinal direction) at the side faces of K_B specimens [17]. These tensile stresses, measured using synchronous X-ray microdiffraction techniques, counterbalance the compressive residual stress field under the indentation,

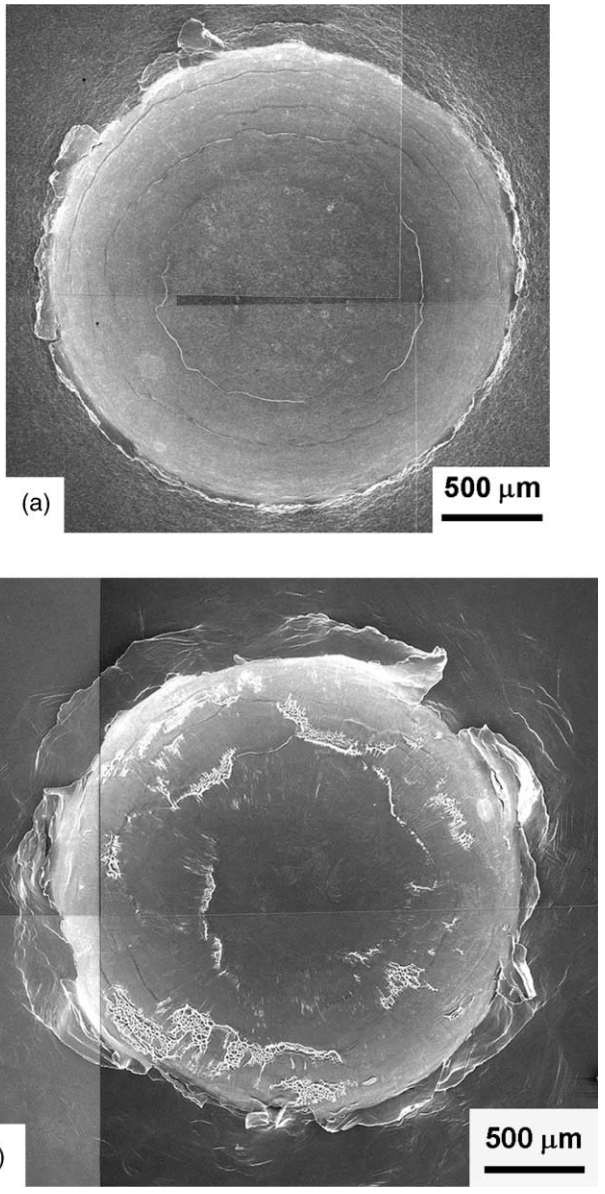

Fig. 2. Scanning electron micrographs of impact damage sites (300 m/s impact velocity) for (a) bi-modal and (b) lamellar microstructure of Ti–6Al–4V. Lamellar microstructure showed increased damage with respect to pile-up formation at crater rim and intense shear band formation emanating at the indent surface.

as numerically analyzed by Chen and Hutchinson [18] and measured by Boyce et al. [17].

3.2. Fatigue properties and FOD-induced crack initiation

The fatigue life of undamaged smooth-bar specimens was markedly reduced by prior high-velocity impact damage, as clearly illustrated by the stress-life (S–N) data in Fig. 4. This reduction was found at both low- and high-load ratios (R=0.1 and 0.5) in both microstructures. Basically, two groups of failures could be identified. At high applied stresses (relative to the magnitude of the tensile residual stresses) and high impact velocities, where large impact-induced microcracks are formed (surface crack lengths are indicated at individual data points), failures initiated from impact-induced cracks at the crater rim. Micrographs of the failed samples are shown in Fig. 5(a) and (b) for the bi-modal and lamellar microstructures, respectively. For lower velocity impacts under these conditions, fatal cracks initiated at the base of the indent site because of the higher stress concentration there compared to that at the crater rim [7]. In contrast, at lower applied stresses and lower impact velocities, where the impact-induced microcracks were absent or much smaller, fatigue cracks were found to initiate in regions of relatively high tensile residual stresses, away from the indent crater, see Fig. 6.

3.3. Fatigue thresholds and crack propagation

Thresholds for fatigue-crack growth and the subsequent near-threshold fatigue-crack growth rates were measured on all FOD-impacted samples and are compared in Fig. 7(a) (R=0.1) and Fig. 7(b) (R=0.5) with results for through-thickness large (>5 mm) cracks in undamaged material [5,19]. The FOD-initiated crack growth rate data are shown as a function of surface crack length, 2c, and the approximate applied stress-intensity range (corrected for the stress concentration of the indent using Eq. (1)). For the FOD-induced microcracks, which are truly microstructurally small cracks, growth-rate data points for both microstructures fall into a single scatter band. Similarly, growth-rate data points for both load ratios (R=0.1 and 0.5) fall into a single scatter band, indicating the controlling effect of the alternating, rather than the mean, stresses. In general, the growth rates of the FOD-initiated small cracks in both microstructures were at least an order of magnitude faster than the corresponding large-crack results at near-threshold levels; such an effect is typical for microstructurally small cracks [10,20–23]. However, the large and small crack results tend to merge above a ΔK of ~10 MPa $m^{1/2}$ for the bi-modal microstructure, consistent with the increased dimensions of the small cracks. This is in contrast to the lamellar microstructure, which exhibits much higher crack-growth resistance than the bi-modal microstructure in the presence of large through-thickness cracks. Because of the larger characteristic microstructural size-scales in this condition, cracks of millimeter dimensions apparently can still display a small crack effect.

One factor associated with the faster growth rates of the FOD-initiated microcracks is the microstructural changes associated with impact-induced plasticity. This is evident from shot-peening experiments on Ti–6Al–4V where, by separating the effect of deformation from residual stresses, it was observed that the deformed microstructure showed drastically reduced resistance to

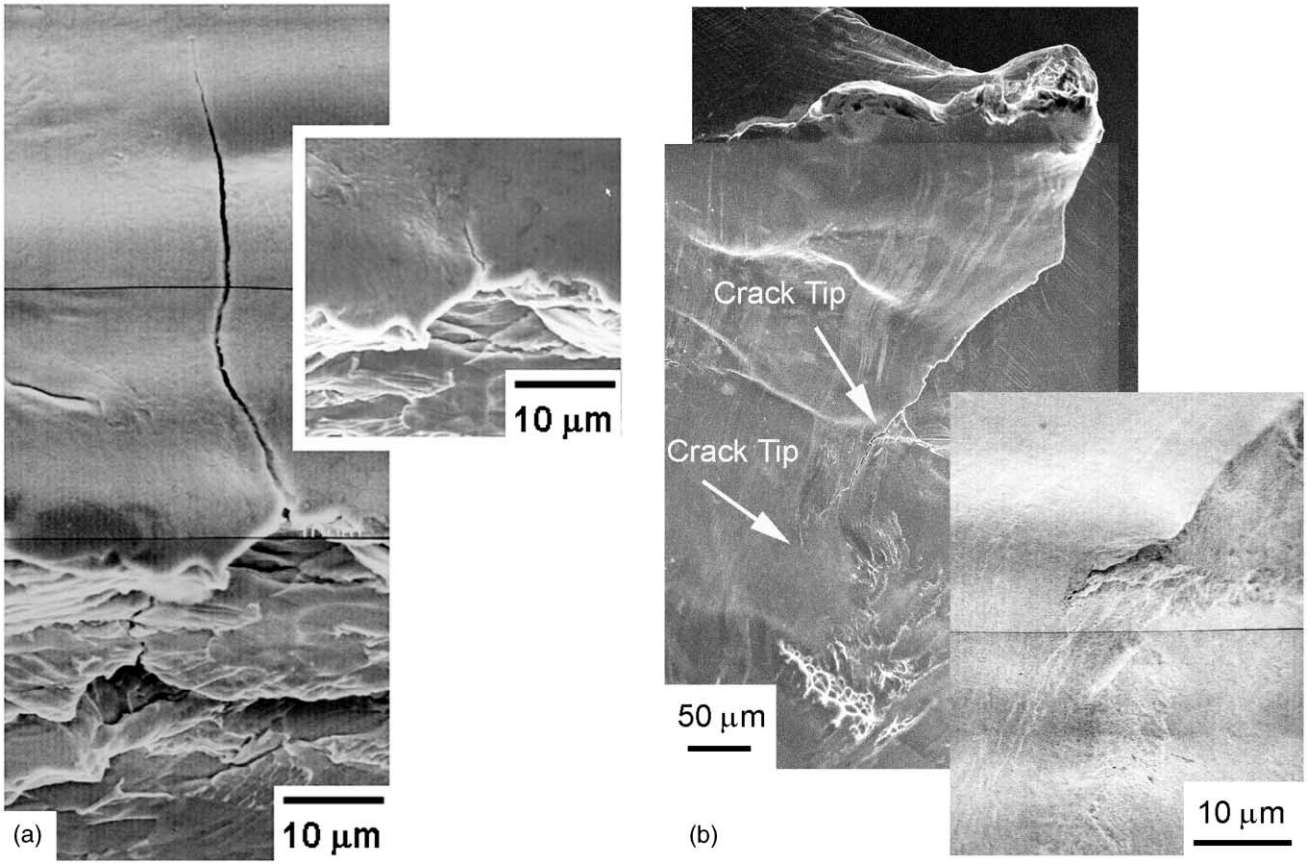

Fig. 3. Examples of fatigue cracks that formed at FOD-induced microcracks (small inserts). (a) Bi-modal microstructure (nominally applied σ_{max}=500 MPa, R=0.1, N=29,000 cycles) and (b) lamellar microstructure (nominally applied σ_{max}=500 MPa, R=0.1, N=3000 cycles).

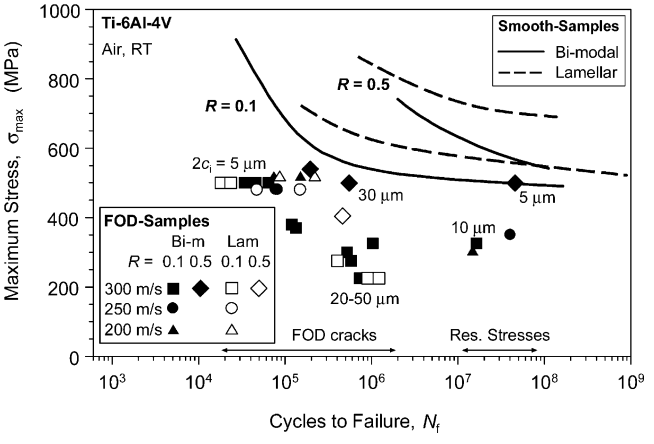

Fig. 4. S–N data (R=0.1 and 0.5) show reduced fatigue life due to simulated FOD as compared to smooth-bar specimens in bi-modal and lamellar Ti–6Al–4V. $2c_i$ is the surface crack length of FOD-induced microcracks. Bi-modal smooth-bar data (N_f<2×10^7 cycles) taken from [13].

crack growth [24,25]. However, the principal factor is associated with the small crack effect.

As discussed elsewhere [5,19], the large-crack thresholds shown in Fig. 7 were determined up to the highest load ratios (R~0.91–0.95) under conditions (constant-K_{max}/increasing-K_{min}) chosen to minimize the effect of crack closure. Accordingly, for the bi-modal microstructure, the threshold of ~1.9 MPa m$^{1/2}$ at R=0.95 is considered to be a worst-case threshold for cracks of dimensions that are larger compared to the scale of the bi-modal microstructure, i.e. for continuum-sized cracks. Similarly, a worst-case threshold of ~3.3 MPa m$^{1/2}$ at R=0.91 was measured for continuum-sized cracks in the lamellar microstructure [19]. However, observations show that the smallest FOD-initiated cracks, which have dimensions comparable with microstructural size-scales, i.e. ~2–10 μm, can propagate at stress intensities well below these worst-case thresholds, specifically at applied stress intensities as low as ΔK~1 MPa m$^{1/2}$, presumably due to biased sampling of the 'weak links' in the microstructure.

Based on the results shown in Fig. 7(a) (R=0.1) and Fig. 7(b) (R=0.5), it is clear that a concept of a worst-case threshold (determined under $R\rightarrow1$ conditions that minimize crack closure) applies strictly for continuum-sized cracks. This concept does not provide lower-bound threshold stress intensity for cracks on the scale of microstructural dimensions, as in the earliest stages of FOD-induced fatigue failure in bi-modal microstructure

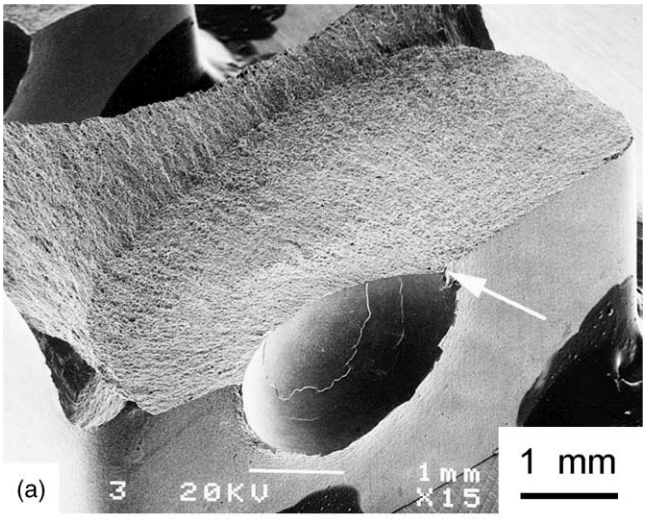

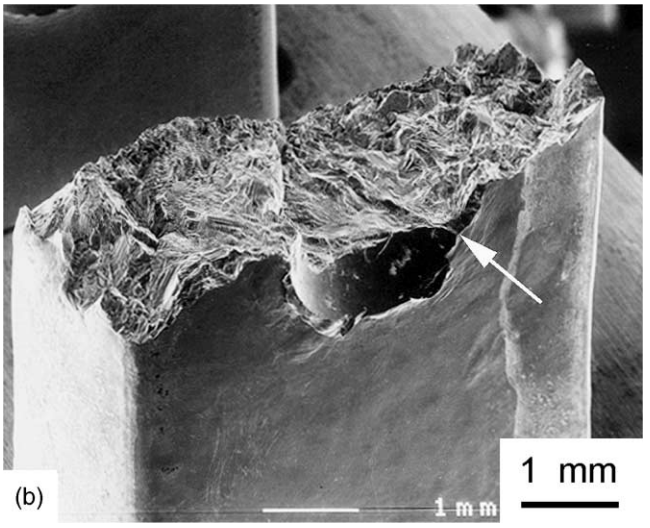

Fig. 5. At high applied stresses relative to the magnitude of the tensile residual stresses and high impact velocities (300 m/s), where large impact-induced microcracks are formed, failures initiated from impact-induced cracks at the crater rim (marked by arrows): (a) bi-modal microstructure (nominally applied σ_{max}=500 MPa, R=0.1, N_F=65,000 cycles) and (b) lamellar microstructure (nominally applied σ_{max}=500 MPa, R=0.1, N_F=23,000 cycles).

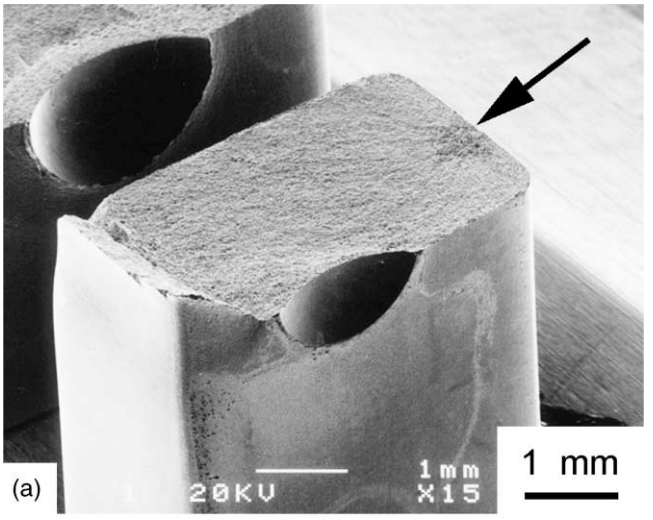

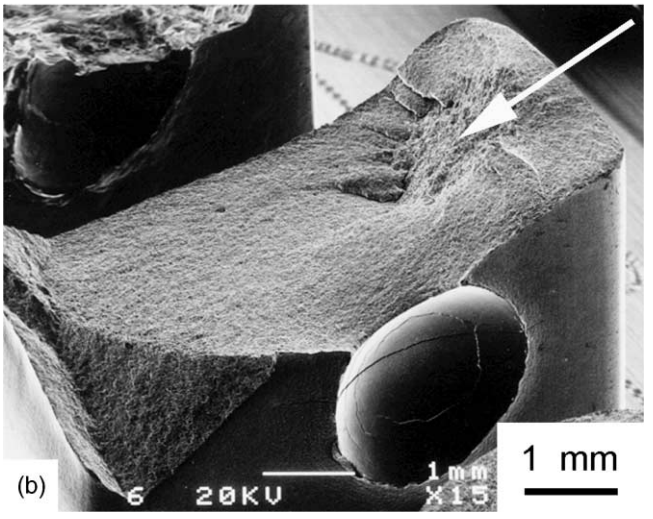

Fig. 6. At lower applied stresses and lower impact velocities, where impact-induced microcracks are much smaller or absent, failures initiated in regions of relatively high tensile residual stresses away from the indents (marked by arrow): (a) fatigue crack initiated close to the surface for 200 m/s impact (bi-modal microstructure, nominally applied σ_{max}=325 MPa, R=0.1, N_F=1.5×10^7 cycles) and (b) less common case of fatigue crack initiation in the interior for 300 m/s high velocity impact (bi-modal microstructure, nominally applied σ_{max}=325 MPa, R=0.1, N_F=1.6×10^7 cycles).

and even at later stages, e.g. for larger crack sizes, in lamellar microstructure.

3.4. Threshold conditions based on the Kitagawa–Takahashi diagram

For the fine-grained bi-modal microstructure, coupling the concept of the worst-case threshold stress intensity with the 10^7-cycle fatigue limit, as in the Kitagawa–Takahashi diagram [11], has been shown to provide an alternative approach to defining limiting conditions for HCF and FOD-related damage [7,10]. The Kitagawa–Takahashi diagram essentially describes a failure envelope, given by the smooth-bar fatigue limit and the fatigue crack growth threshold, usually measured on fracture mechanics type specimens. The influence of crack size on the stress range conditions for no crack growth (da/dN=10^{-11}–10^{-10} m/cycle) in the form of a modified Kitagawa–Takahashi diagram is shown for the bi-modal (closed symbols) and lamellar microstructures (open symbols) in Fig. 8(a) for applied load ratios of R=0.1 and in Fig. 8(b) for R=0.5.

The results of the bi-modal microstructure (closed symbols and solid lines) show that crack growth at both R-ratios from FOD-induced microstructurally small

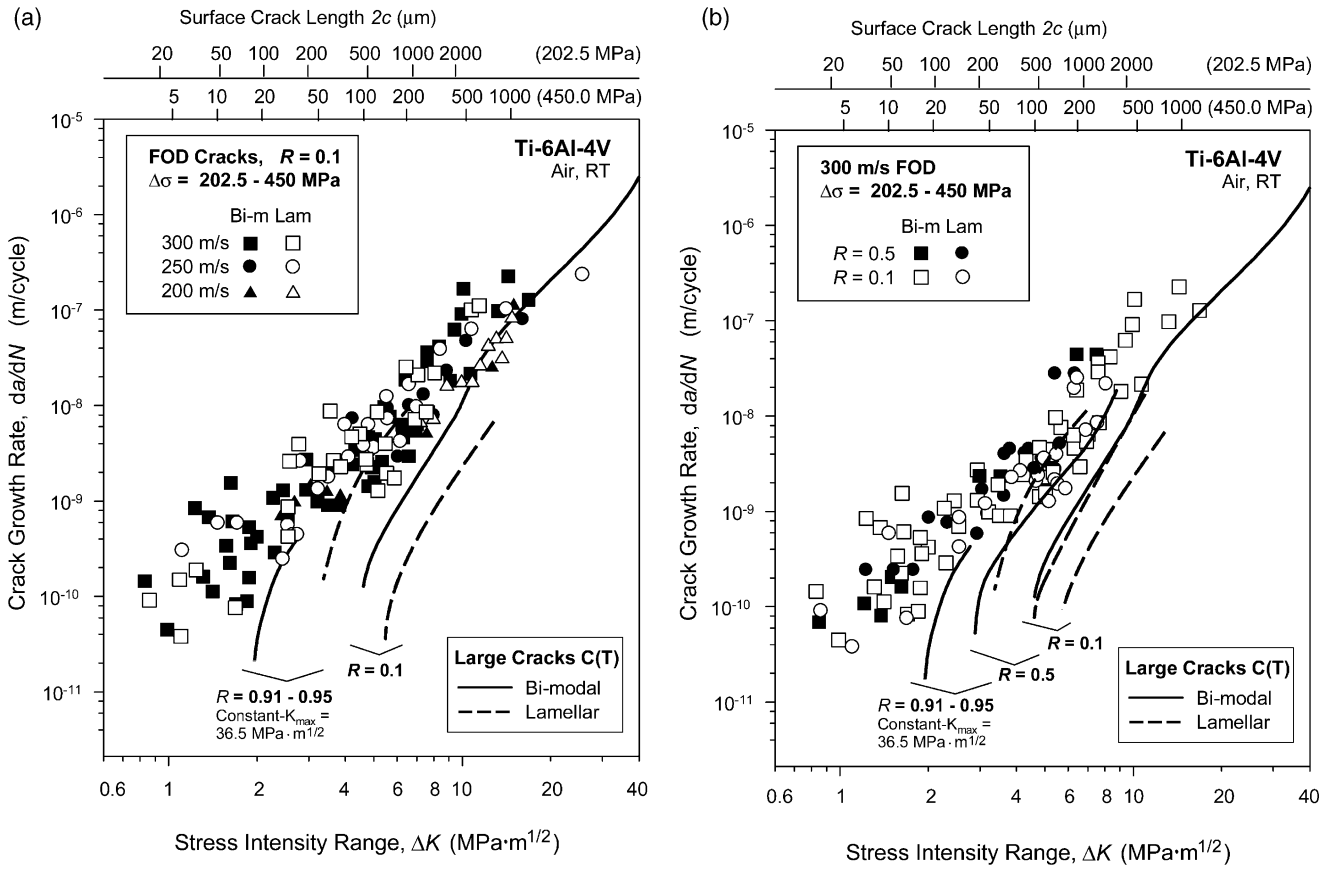

Fig. 7. Crack-growth rates as a function of applied stress-intensity range at load ratios of (a) R=0.1 and (b) R=0.1 and 0.5 of FOD small cracks and through-thickness large cracks in bi-modal and lamellar Ti–6Al–4V. Large-crack growth data for R=0.1 were derived from constant load-ratio tests, whereas for R=0.91 (lamellar) and 0.95 (bi-modal) constant-K_{max}/increasing-K_{min} testing was used [5,19].

cracks can be described by the stress-concentration corrected fatigue limit at relatively high applied stress ranges and by the worst-case threshold for larger continuum-sized cracks at lower stress ranges, Fig. 8(a) (R=0.1) and Fig. 8(b) (R=0.5). However, for failures in the presence of low applied stresses relative to tensile residual stresses, the effective R-ratio in the Kitagawa–Takahashi diagram has to be corrected for the presence of such residual stresses, as discussed below.

In the presence of low applied stress ranges relative to the tensile residual stresses in the vicinity of the damage sites, fatigue cracks were seen to be initiated in regions away from the indents (Fig. 6); specifically, they tended to initiate in regions of high tensile residual stress (oriented parallel to applied stresses). Fatigue crack initiation was generally found close to the side faces (Fig. 6(a)) of the rectangular gauge section, where tensile residual stresses of ~300 MPa have been measured. A less common case of fatigue crack initiation in the interior for 300 m/s high-velocity impact is shown in Fig. 6(b). Data from these fatigue failures are plotted in Fig. 8(a) and (b) at surface crack lengths of $2c$=1 μm. Tensile residual stresses of ~300 MPa significantly affect the mean stress and hence in this case increase the R-ratio of 0.1 to 0.5 (far-field stress range of ~300 MPa). However, it can be seen in Fig. 8(c) that provided such residual stresses are accounted for, such failures at both R=0.1 and 0.5 can still be described by the proposed Kitagawa–Takahashi approach, provided the limited conditions are given by the residual stress corrected smooth-bar fatigue limit for small crack sizes and worst-case threshold for larger crack sizes.

It should be noted that the failure envelopes in Fig. 8(a)–(c) can be somewhat better represented by the El Haddad et al. [26] empirical quantification of Kitagawa–Takahashi approach. This approach introduces a constant, termed the intrinsic crack length, $2c_o$, such that the stress intensity is defined as $\Delta K=Y\Delta\sigma\sqrt{\pi(2c+2c_o)}$, where Y is the geometry factor.

Corresponding threshold conditions for the lamellar microstructure are shown in the context of the Kitagawa–Takahashi approach by the results (open symbols and dashed lines) in Fig. 8(a) (R=0.1) and Fig. 8(b) (R=0.5). This coarser structure has a significantly better resistance to large-crack growth in the form of a ~75% higher worst-case threshold, and a greater resistance to crack initiation in the form of a higher smooth-bar fatigue strength. However, the lamellar structure was

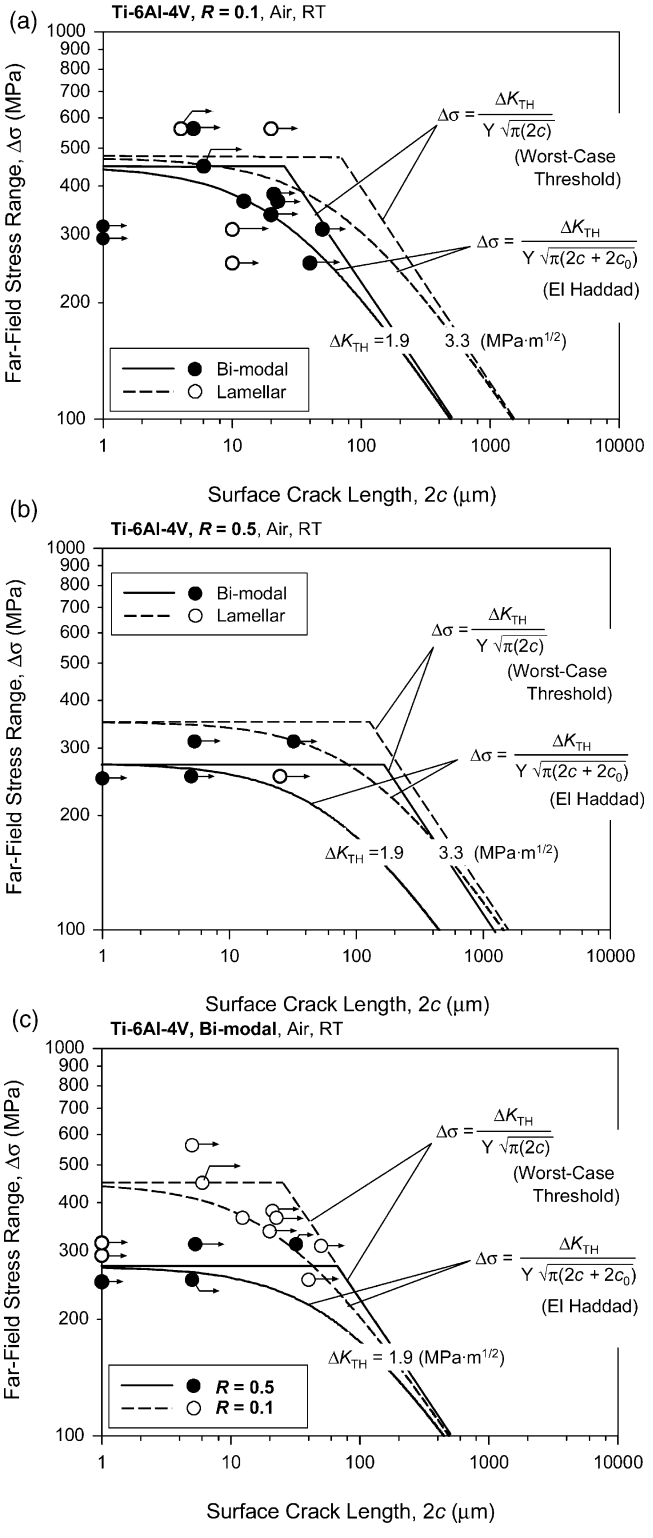

Fig. 8. Modified Kitagawa-Takahashi diagram representing the threshold crack-growth conditions (da/dN=10^{-11}–10^{-10} m/cycle) at (a) R=0.1 and (b) R=0.5 for FOD-induced small-cracks in bi-modal and lamellar Ti–6Al–4V; (c) shows data for bi-modal microstructure at both R=0.1 and 0.5. Plotted is the threshold stress range as a function of surface crack length. Data points are corrected for the stress concentration of the FOD indents.

more prone to the formation of FOD-induced microcracks, although there was little difference in the HCF properties of the two microstructures in the presence of such microcracks, i.e. small-crack growth rates were essentially identical in the two structures. In general though, as the proposed Kitagawa–Takahashi approach is based on the limiting large-crack threshold and smooth-bar fatigue limit, the approach is somewhat less suited for FOD-induced failures in the lamellar microstructure. This is because the small-crack growth resistance, which controls such failures, is comparatively so much lower than that shown by large cracks in this structure; moreover, measured smooth-bar fatigue limits can be artificially inflated due to the much coarser microstructure which restricts the sampling of microstructural 'weak links' in specimens of finite size.

4. Summary and conclusions

Based on a study of the influence of microstructure on FOD and resulting thresholds for HCF in bi-modal and lamellar microstructures in a Ti–6Al–4V alloy, the following conclusions can be made:

1. FOD, simulated by high-velocity (200–300 m/s) impacts of steel spheres on a flat surface, was found to markedly reduce resistance to HCF in both bi-modal and lamellar microstructures. Principally, the effect of FOD was to induce preferred sites for the premature initiation of fatigue cracks on subsequent cycling.
2. Premature crack initiation resulted from (1) the stress concentration due to the FOD indentation, (2) presence of (microstructurally small) microcracks at the crater rim of the damaged zone (seen only at the highest impact velocities), (3) localized presence of tensile residual stresses, and (4) microstructural damage from FOD-induced plastic deformation.
3. For lower velocity impacts (200 m/s), neither such microcracking at the crater rim, nor circumferentially orientated shear bands emanating from the surface of the crater, could be detected. This strongly implies that low velocity or quasi-static indentations do not necessarily provide a realistic simulation of high-velocity FOD.
4. At *stress-concentration corrected* stress ranges from 250 to 560 MPa, FOD-initiated microcracks (~2–10 μm in size) propagated at applied stress intensities even below ΔK=1 MPa $m^{1/2}$ (at both R=0.1 and 0.5) and showed no pronounced threshold behavior, i.e. small-crack growth occurred at driving forces well below the worst-case ΔK_{TH} threshold of 1.9 MPa $m^{1/2}$ (bi-modal) and 3.3 MPa $m^{1/2}$ (lamellar microstructure) for continuum-sized cracks (i.e. cracks larger than the characteristic microstructural

size-scales) in this alloy. Furthermore, such FOD-induced fatigue cracks propagated at rates at least an order of magnitude faster than corresponding large (>5 mm) cracks at the same applied stress-intensity range.

5. The critical condition for HCF in the bi-modal and lamellar Ti–6Al–4V in the presence of continuum-sized cracks could be defined in terms of the worst-case fatigue threshold (determined under $R \rightarrow 1$ conditions that minimize crack closure). However, this concept alone is inappropriate where microstructurally small cracks are present.
6. For FOD-initiated failures, where the critical condition for HCF must be defined in the presence of microstructurally small cracks, the Kitagawa–Takahashi diagram represents a more appropriate approach, where the limiting conditions are defined in terms of the worst-case ΔK_{TH} fatigue threshold (at large continuum-sized crack sizes) and the 10^7-cycle fatigue limit (at small cracks sizes), with corrections for the stress concentration of the indent and the presence of residual stresses (which affect the effective load ratio).

Acknowledgements

This work was supported by the Air Force Office of Science and Research, Grant No. F49620-96-1-0478, under the Multidisciplinary University Research Initiative on 'High Cycle Fatigue' to the University of California, Berkeley. Special thanks are due to Prof. Werner Goldsmith (UCB) for providing the compressed-gas gun facility and to Prof. J.W. Hutchinson, Dr J.M. McNaney and Dr A.W. Thompson for helpful discussions, and to B.L. Boyce, R.K. Nalla, and Xi Chen for providing us with their results prior to publication, and to J.L. Hendricks and C.K. Lau for their help with scanning electron microscopy.

References

[1] Cowles BA. High cycle fatigue in aircraft gas turbines — an industry perspective. Int J Fracture 1996;80:147–63.
[2] Nicholas T, Zuiker JR. On the use of the Goodman diagram for high cycle fatigue design. Int J Fracture 1996;80:219–35.
[3] Larsen JR, Worth BD, Annis CG Jr., Haake FK. An assessment of the role of near-threshold crack growth in high cycle fatigue life prediction of aerospace titanium alloys under turbine engine spectra. Int J Fracture 1996;80:237–55.
[4] Ritchie RO. Small cracks and high-cycle fatigue. In: Chang JCI, Coulter J, Brei D, Martinez WHG, Friedmann PP, editors. Proceedings of the ASME Aerospace Division, AD-Vol. 52, ASME, Warrendale, PA, 1996:321–33.
[5] Ritchie RO, Davidson DL, Boyce BL, Campbell JP, Roder O. High-cycle fatigue of Ti–6Al–4V. Fatigue Fract Eng Mat Struct 1999;22:621–31.
[6] Peters JO, Roder O, Boyce BL, Thompson AW, Ritchie RO. Role of foreign-object damage on thresholds for high-cycle fatigue in Ti–6Al–4V. Metall Mater Trans A 2000;31A:1571–83.
[7] Peters JO, Ritchie RO. Influence of foreign-object damage on crack initiation and early crack growth during high-cycle fatigue of Ti–6Al–4V. Eng Fract Mech 2000;67A:193–207.
[8] Nicholas T, Barber JR, Bertke RS. Impact damage on titanium leading edges from small hard objects. Exp Mech 1980;October:357–64.
[9] Hudak SJ, Chan KS, McClung RC, Chell GG, Lee Y-D, Davidson DL. High cycle fatigue of turbine blade materials. Final technical report UDRI Subcontract No. RI 40098X SwRI Project No. 18-8653, 1999.
[10] Ritchie RO, Peters JO. Small fatigue cracks: mechanics, mechanisms and engineering applications. Mater Trans 2001;42:58–67.
[11] Kitagawa H, Takahashi S. Applicability of fracture mechanics to very small cracks or the cracks in the early stage. In: Proceedings of the Second International Conference on Mechanical Behavior of Materials. Metals Park (OH): ASM, 1976:627–31.
[12] Eylon D. Summary of the available information on the processing of the Ti–6Al–4V HCF/LCF program plates. University of Dayton report, Dayton (OH), 1998.
[13] Hines JA, Peters JO, Lütjering G. Microcrack propagation in Ti–6Al–4V alloys. In: Boyer RR, Eylon D, Lütjering G, editors. Fatigue behavior of titanium alloys. Warrendale (PA): TMS, 1999:15–22.
[14] Lukáš P. Stress intensity factor for small notch-emanating cracks. Eng Fract Mech 1987;26:471–3.
[15] Nisida M, Kim P. Stress concentration caused by the presence of a spherical cavity or a spherical-surfaced hollow. In: Proceedings of the Twelfth National Congress Applied Mechanics, 1962:69–74.
[16] Newman JC Jr., Raju IS. An empirical stress-intensity factor equation for the surface crack. Eng Fract Mech 1981;15:185–92.
[17] Boyce BL, Chen X, Hutchinson JW, Ritchie RO. The residual stress state due to a spherical hard-body impact. Mech Mater 2001;33:441–54.
[18] Chen X, Hutchinson JW. Foreign object damage and fatigue crack threshold: cracking outside shallow indents. Int J Fract 2001;107:31–51.
[19] Nalla RK, Campbell JP, Ritchie RO. Mixed-mode high-cycle fatigue thresholds in Ti–6Al–4V: a comparison of large and small crack behavior. In: Proceedings of the Sixth International Conference on Biaxial/Multiaxial Fatigue and Fracture, Lisbon, Portugal, 2001.
[20] Suresh S, Ritchie RO. Propagation of short fatigue cracks. Int Metals Rev 1984;29:445–76.
[21] Miller KJ, de los Rios ER. The behaviour of short fatigue cracks. Mechanical Engineering Publications, London, UK, 1986.
[22] Ritchie RO, Lankford J. Small fatigue cracks. Warrendale, PA: TMS-AIME, 1986.
[23] Ravichandran KS, Ritchie RO, Murakami Y. Small fatigue cracks: mechanics, mechanisms and applications. Oxford, UK: Elsevier, 1999.
[24] Wagner L, Lütjering G. Influence of shot peening parameters on the surface layer properties and the fatigue life of Ti–6Al–4V. In: Fuchs HO, editor. Proceedings of the Second International Conference of Shot Peening. Paramus (NJ): American Shot Peening Society, 1984:194–200.
[25] Wagner L, Lütjering G. Influence of a shot peening treatment on the fatigue limit of Ti–6Al–4V. In: Fuchs HO, editor. Proceedings of the Second International Conference Shot Peening. Paramus (NJ): American Shot Peening Society, 1984:201–7.
[26] El Haddad MH, Topper TH, Smith KN. Prediction of non propagating cracks. Eng Fract Mech 1979;11:573–84.